

## RESEARCH ARTICLE

# Co-simulation approach for computational aero-acoustic modeling: Investigating wind-induced noise within two-way radio microphone ports cavity

W. M. Hairudin<sup>1\*</sup>, M. N. H. Mat<sup>2</sup>, L. E. Ooi<sup>3</sup> and N. A. Ismail<sup>1</sup>

<sup>1</sup> School of Aerospace Engineering, Engineering Campus, Universiti Sains Malaysia, 14300 Nibong Tebal, Pulau Pinang, Malaysia  
 Phone: +604-5995901; Fax: +604-5996911

<sup>2</sup> School of Mechanical Engineering, Faculty of Engineering, Universiti Teknologi Malaysia, 81310 UTM, Johor Bahru, Malaysia

<sup>3</sup> School of Mechanical Engineering, Engineering Campus, Universiti Sains Malaysia, 14300 Nibong Tebal, Pulau Pinang, Malaysia

**ABSTRACT** - Wind-induced noise (aeroacoustic) can cause problem with any outdoor microphone applications, notably impacting the performance of telecommunication mobile. One prominent source in two way radios is the microphone port cavity. In this article, the noise characteristics behaviour is studied at scale-up of microphone port cavity through computational aero-acoustics numerical simulation and experimental test. This research aims to investigate the wind-induced noise generated inside the microphone port cavity at various wind orientation angles and distance radii,  $r$ . A direct-hybrid co-simulation CAA method, utilizing the wall-adapting local eddy-viscosity and Ffowcs William-Hawking models, is employed to obtain the near-field noise source and far-field noise patterns inside a microphone port cavity. The simulations are conducted using the scFLOW2Actran software. Richardson extrapolation and grid convergence index are applied to evaluate the accuracy of the grid independency in numerical simulations. The findings reveal that the leading edge, centre and trailing edge are the primary noise sources and generations inside a microphone port. The study indicates that the noise level in the microphone port cavity is characterized by low frequency noise. The results indicate that at an observation of angles of  $0^\circ$  and distance radii of 0.2 m, the wind noise level is higher compared to other orientation angle and distance radii. This can be attributed to the proximity to the noise source at this location. The directivity pattern of noise propagation exhibits a typical dipole pattern observed at observation angles of  $0^\circ$  to  $45^\circ$ . Numerical results align well with the experimental results from the wind tunnel test, demonstrating the feasibility of the proposed approach for flow-acoustic coupling application. This research holds significant value for engineers as it provides a comprehensive understanding of the physical phenomena involved in microphone port design.

## ARTICLE HISTORY

Received : 23<sup>rd</sup> Aug. 2023

Revised : 26<sup>th</sup> Nov. 2023

Accepted : 19<sup>th</sup> Jan. 2024

Published : 30<sup>th</sup> Mar. 2024

## KEYWORDS

*Two-way radio*

*Microphone port*

*Wind-induced noise*

*Aeroacoustics*

*Computational aero-acoustics*

## 1. INTRODUCTION

Telecommunication devices, including hearing aids, microphones, headsets, or even two-way radios frequently encounter wind-induced noise during outdoor use. This noise can be disruptive, especially in windy situations. Wind-induced noise in a microphone originates from two main sources: (1) flow turbulence, which naturally produces vortices and fluctuations, and (2) turbulence caused by wind interacting with open surfaces or gaps of the devices, known as microphone port cavity [1]. Despite the incorporation of noise-canceling algorithms and digital signal processing (DSP) by mobile communication manufacturers [2,3], there is a limited understanding of wind-induced noise generation and propagation specifically in the microphone port cavity of two-way radios. The exploration of flow and acoustics within the cavities of electronic devices, such as two-way radios remains a relatively new area of study [4].

Cavity structure is widely used in various applications, such as landing gear bay of aircraft [5-8], sunroofs in cars [9,10], and the pantograph cavity of high-speed trains [11,12]. The primary noise source in these applications is aerodynamic noise generated by the interaction between the cavity and incoming flow is the main noise source of this application. Existing literature primarily focuses on open and rectangular cavities in high-speed flow such as that found in aircraft and automotive sectors. However, there are some cases where the cavity is incorporated into a small electronic device facing a low wind speed. For example, the existence of wind-induced noise in a small cavity inside the electronic device [13-15]. Research has predominantly concentrated on aeroacoustic investigation in the cavity of telecommunication devices. Fisol [13] demonstrated that vorticity is generated in the vicinity of the open cavity, considered as a primary noise source. The study indicates that the sound pressure increases with higher wind velocities and cavity distances. It indicates that the cavity position of P5 was identified for reducing wind-induced noise. However, it did not provide the noise level in decibels (dB) for each case. Hairudin et al. [16] conducted a similar investigation using ANSYS Fluent, exploring the effect of cavity position and Reynolds number. The computational fluid dynamic (CFD) results revealed the presence of shear layer separation, and discrete vortices at the leading and trailing edges of the

cavity. Saw et al. [17] patented adjustments inside the microphone port, resulting in a 5 dB reduction of wind noise compared to the previous design. However, detailed experimental methods were not discussed. Hairudin et al. [18] performed a wind tunnel test to investigate the effect of cavity position on noise levels, demonstrating that the farthest position resulted in minimal wind noise levels. In another study, Hairudin et al. [19] used flow visualization method to examine the flow structure produced under different cavity length-to-depth (L/D) ratios of microphone ports through wind tunnel testing. The results indicated that microphone ports with a small L/D ratio produced a single vortex shedding, while those with larger L/D ratios exhibited multiple vortices. These vortices had an impact on the noise level, showing limited studies focus on the aeroacoustic analysis of the wind-induced noise inside a microphone port. It addresses the relatively unexplored area of the interaction between wind and cavity surfaces of the electronic device.

Empirical and experimental methods have long been pioneers in this field, but their reliance on expensive equipment and facilities poses implementation challenges [20]. With the rapid advancement in computer technology and numerical methods, computational aero-acoustic (CAA) has become increasingly prevalent in obtaining flow field and acoustic characteristics. CAA serves as a numerical computational tool to extract acoustic data from flow field results. In the analysis of wind-induced noise, two primary methods are employed; direct CAA [21,22], and the hybrid CFD/CAA method [23-28]. Direct numerical simulation (DNS) faces challenges due to the vast scale disparity between flow-acoustic phenomena and the computational time required, making its practical implementation difficult and expensive [29]. However, the hybrid CFD/CAA method while more practical, involves two steps and the utilization of different software tools [30]. Nonetheless, the hybrid CFD/CAA method has limitations including increasing data storage requirements and sequential execution of CFD and CAA solvers, which may potentially affect accuracy, computational efficiency, and data management [31].

To overcome these drawbacks, the direct-hybrid co-simulation CAA method has been introduced to compute aeroacoustic sources within the CFD. These sources can then predict the noise generation and propagation simultaneously within a single computational framework. The direct-hybrid co-simulation CAA approach, in comparison to methods like RANS, DNS, and hybrid CFD/CAA presents notable advantages. Firstly, it offers a simultaneous solution to both CFD for the flow field and acoustic field within a unified computational domain., eliminating the need for two separate solvers of software applications. Additionally, it excels in simplicity by eliminating the explicit coupling interfaces and enables concurrent execution without the need for disk I/O, streamlining data exchange and storage processes. The direct-hybrid co-simulation used in this study is a relatively new approach in CAA applications, compared to previous hybrid CFD/CAA studies.

The main aims of this work are to analyze the noise source and the noise radiated within a microphone port cavity at various orientation angles (wind direction), and distance radii in both near-field and far-field regions using a direct-hybrid co-simulation CAA method. The proposed direct-hybrid co-simulation CAA method is validated through comparisons with corresponding experimental test results. This research provides a valuable reference for acoustic researchers and engineers in designing other devices and mitigating wind-induced noise.

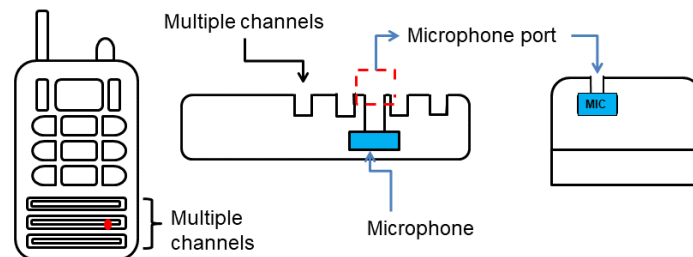


Figure 1. Schematic diagram of the cross-section of microphone port cavity within a two-way radio

## 2. MATERIALS AND METHODS

Each governing equation corresponds to the respective solution incorporated in the scFLOW2Actran software. These equations are meticulously detailed for aeroacoustics analysis solution. To simulate the wind-induced noise (aeroacoustics), a direct-hybrid two-step approach is employed. The first step involves a CFD simulation, capturing the physics of the underlying flow field. The second step addresses the sound propagation (acoustic) within the microphone port. The governing equations include the hybrid Reynolds-Averaged Navier Stokes (RANS)  $k - \omega$  SST, Wall-Adapting Local Eddy Viscosity (LES-WALE), and the Ffowcs William-Hawking (FW-H) acoustic analogy. The LES\_WALE and Ffowcs William Hawking models are versatile and widely used in aeroacoustics simulation. They can be applied in various applications such as aircraft noise [32, 33], wind turbine [34-36], automotive noise [37], and underwater acoustic [38-41].

### 2.1 Governing Equation for Steady-State Flow: Reynolds Average Navier Stokes

The governing equations for the flow field around the microphone port are based on the incompressible Navier-Stokes equations. These equations describe the behavior of the fluid flow in a steady-state CFD simulation, encompassing the conservation of mass and momentum. The equation is as follows:

Conservation of continuity:

$$\frac{\partial u_i}{\partial x_i} = 0 \tag{1}$$

Conservation of momentum:

$$\rho \frac{\partial u_i}{\partial t} + \rho \frac{\partial (u_i u_j)}{\partial x_j} = \frac{\partial \tau_{ij}}{\partial x_j} - \frac{\partial p}{\partial x_i} + \rho f_i \tag{2}$$

where subscripts  $i, j = 1, 2, x_i$  and  $x_j$  denote the physical space directions,  $\rho$  is the fluid density,  $v$  is the velocity,  $p$  is the fluid pressure,  $u_i$  and  $u_j$  are the time-averaged velocity components,  $f_i$  is the external forces, and the stress tensor:

$$\tau_{ij} = \mu \left( \frac{\partial u_i}{\partial x_j} + \frac{\partial u_j}{\partial x_i} \right) \tag{3}$$

where  $\mu$  denotes the dynamic viscosity. The Reynolds Average Navier Stoke RANS  $k - \omega$  shear stress transport turbulence model, as developed by [42] is widely utilized as a turbulence closure model in CFD simulations [31, 43]. This model is employed to enhance separation in the near-wall region and has demonstrated good prediction capabilities for adverse pressure gradient and flow separation [44, 45]. The turbulence properties of the flow are represented by turbulent kinetic energy,  $k$ , and dissipation rate,  $\omega$ . The equations are expressed as;

Turbulence kinetic energy,  $k$

$$\frac{D\rho k}{Dt} = \pi_{ij} \frac{\partial u_i}{\partial x_j} - \beta^* \rho \omega k + \frac{\partial}{\partial x_j} \left[ (\mu + \sigma_k \mu_t) \frac{\partial k}{\partial x_j} \right] \tag{4}$$

Turbulent dissipation,  $\omega$

$$\frac{D\rho \omega}{Dt} = \pi_{ij} \frac{\gamma}{v_t} - \beta \rho \omega^2 k + \frac{\partial}{\partial x_j} \left[ (\mu + \sigma_w \mu_t) \frac{\partial \omega}{\partial x_j} \right] + 2\rho(1 - F_1) \rho \sigma_{\omega 2} \frac{1}{\omega} \frac{\partial k}{\partial x_i} \frac{\partial \omega}{\partial x_j} \tag{5}$$

where  $\mu_t$  is the kinematic viscosity and given as:

$$v_t = \frac{a_1 k}{\max(a_1 \omega, \Omega F_2)} \tag{6}$$

Here,  $\Omega$  represents the absolute value of vorticity. The following closure coefficient of  $F_1$  and  $F_2$  of this study are described as:

$$F_2 = \tanh \left[ \left[ \max \left( 2 \frac{\sqrt{2}}{0.09 \omega y}, \frac{500 v}{y^2 \omega} \right) \right]^2 \right] \tag{7}$$

$$F_1 = \tanh \left[ \min \left[ \max \left( 2 \frac{\sqrt{k}}{0.09 \omega y}, \frac{500 v}{y^2 \omega} \right), \frac{4 \rho \sigma_{\omega 2} k}{CD_{k\omega} y^2} \right]^4 \right] \tag{8}$$

where  $y$  is the distance to the next surface,  $CD$  is the positive part of the diffusion term in Eq. (4);

$$CD_{k\omega} = \max \left( 2 \rho \sigma_{\omega 2} \frac{1}{\omega} \frac{\partial k}{\partial x_j} \frac{\partial \omega}{\partial x_j}, 10^{-20} \right) \tag{9}$$

The constant of  $\phi$  for  $k - \omega$  SST is given in Eq. (9):

$$\phi = \phi_1 F_1 + \phi_2 (1 - F_1) \tag{9}$$

$$\beta_1 = \frac{3}{40}, \beta_2 = 0.0828, \beta^* = \frac{9}{100} \tag{10}$$

$$\sigma_{k1} = 0.85, \sigma_{k2} = 1, \sigma_{w2} = 0.856 \tag{11}$$

## 2.2 Governing Equation for Transient Unsteady Flow: Wall Adapting Local Eddy

The LES-WALE turbulence model [46] is employed in the near-field to capture unsteady turbulence in CFD flow simulation involving time-dependent fluid flow. The transient Navier-Stokes equations extend the steady-state equations by incorporating time derivatives. LES resolves large turbulent structures while modeling smaller ones. The LES-WALE model enhances near-wall behavior by adapting the eddy-viscosity [47]. The governing equation for incompressible LES-WALE is derived from filtered Navier-Stokes and continuity equations [48], summarized as follows:

$$\frac{\partial \bar{u}'_i}{\partial x_i} = 0 \tag{12}$$

$$\rho' \frac{\partial \bar{u}'_i}{\partial t} + \frac{\partial (\bar{u}'_i \bar{u}'_j)}{\partial x_j} = \frac{\partial}{\partial x_j} \left[ \mu \left( \frac{\partial \bar{u}'_i}{\partial x_j} + \frac{\partial \bar{u}'_j}{\partial x_i} \right) \right] - \frac{\partial \tau_{ij}^{SGS}}{\partial x_j} - \frac{\partial \bar{p}}{\partial x_i} + \rho' \bar{f}_i \tag{13}$$

where  $\bar{\rho}$  is the filtered density,  $t$  is the time,  $\bar{u}_i$  is the filtered velocity component in the  $i$ - direction,  $x_i$  is the spatial coordinate in  $i$  – direction,  $\bar{p}$  is the filtered pressure,  $\mu$  denotes the dynamic viscosity. The Reynolds subgrid-scale stress (SGS) tensor,  $\tau_{ij}^{SGS}$  [49] reflects the turbulence transport term, signifying turbulent velocity fluctuations. It is solved using the Boussinesq assumption [43,50]. It is also known as filtered stress tensor is written in the following:

$$\tau_{ij}^{SGS} = \rho \bar{u}'_i \bar{u}'_j = \frac{1}{3} \pi_{kk} \delta_{ij} - 2\mu_t \bar{S}_{ij} = \mu_t \left( \frac{\partial \bar{u}'_i}{\partial x_j} + \frac{\partial \bar{u}'_j}{\partial x_i} \right) \tag{14}$$

where  $\delta_{ij}$  is the Kronecker delta tensor,  $\mu_t$  is the turbulent eddy viscosity,  $\bar{S}_{ij}$  is the rate of strain tensor, which can be written as:

$$\mu_t = (C_s \Delta)^2 \sqrt{\bar{S}_{ij} \bar{S}_{ij}} \tag{15}$$

and is the kinematic scale viscosity. This model addresses the limitation of the classical Smagorinsky model [51], which tends to overestimate the SGS viscosity near walls, particularly in high-shear regions [52]. In the WALE model, the turbulent viscosity is modeled as:

$$\mu_t = (C_w \bar{\Delta})^2 \frac{(S_{ij}^d S_{ij}^d)^{3/2}}{(\bar{S}_{ij} \bar{S}_{ij})^{5/2} + (\bar{S}_{ij} \bar{S}_{ij})^{5/4}} \tag{16}$$

where  $S_{ij}^d$  is the traceless symmetric part of the square of the velocity gradient tensor

$$S_{ij}^d = \frac{1}{2} \left( \frac{\partial u_k}{\partial x_i} \frac{\partial \bar{u}_j}{\partial x_k} + \frac{\partial \bar{u}_k}{\partial x_j} \right) - \frac{1}{3} \delta_{ij} \frac{\partial \bar{u}_k}{\partial x_l} \frac{\partial \bar{u}_l}{\partial x_k} \tag{17}$$

$$= \frac{1}{2} (\bar{g}_{ij}^2 + \bar{g}_{ij}^2) - \frac{1}{3} \delta_{ij} \bar{g}_{kk}^2 \tag{18}$$

and  $\bar{g}_{ij}^2 = \bar{g}_{ik} \bar{g}_{kj}$ .  $C_w$  is the model constant and its default value is 0.1 according to Nicoud and Ducros [53].

### 2.3 Governing Equation for Acoustic Model

An extended Lighthill acoustic analogy namely, Ffowcs William-Hawking acoustic analogy [54] is used to predict the far-field noise in a microphone port cavity of two-way radio, respectively. The FW-H acoustic analogy can be expressed as:

$$\frac{1}{c_0^2} \frac{\partial^2 \hat{p}}{\partial t^2} - \nabla^2 = \frac{\partial^2}{\partial x_i \partial x_j} \{T_{ij} H(f)\} - \frac{\partial}{\partial x_i} \{[P_{ij} n_j + \rho u_i (u_n - v_n)] \delta(f)\} + \frac{\partial}{\partial t} \{[\rho_0 v_n + \rho u_i (u_n)] \delta(f)\} \tag{19}$$

where  $u_i$  fluid velocity component in the x-direction,  $u_n$  is the surface velocity component normal to the surface,  $v_i$  is the surface velocity to the x-direction,  $v_n$  is the surface velocity component to the normal surface,  $\delta(f)$  is the Dirac delta function,  $H(f)$  is the Heaviside function,  $\hat{p}$  is the sound pressure at the observation point (far-field),  $\hat{p} = (P - P_0)$ ,  $T_{ij}$  is the Lighthill’s stress tensor,  $T_{ij} = \rho u_i u_j + P_{ij} - c_0^2 (\rho - \rho_0) \delta_{ij}$ ,  $c_0^2$  is the speed of sound, and  $P_{ij}$  is the compressive stress tensor. The compressive stress tensor can be expressed as:

$$P_{ij} = p \delta_{ij} - \mu \left[ \frac{\partial u}{\partial x_j} + \frac{\partial u_j}{\partial x_i} - \frac{2}{3} \frac{\partial u_k}{\partial x_k} \delta_{ij} \right] \tag{20}$$

Green’s function is applied to define the effect of sound sources and acoustic wave propagation from sources to the observation point [55]. Green’s function is utilized to solve the problem Eq. (7). The solution involves both surface and volume integrals [56]. The surface integral represents the contribution of the dipole source to the far-field sound pressure, meanwhile, the volume integrals take into account the volume velocity fluctuations (monopole sources) and the interaction between the mean flow density and vorticity fluctuations (quadrupole sources). However, considering the low Reynolds number is low, the quadrupole sources are neglected [57-59]. Therefore, the complete solution for Eq. (19) can be obtained using Green’s function is expressed as follows:

$$\hat{p}(\vec{x}, t) = \hat{p}_T(\vec{x}, t) + \hat{p}_L(\vec{x}, t) \tag{21}$$

where,

$$4\pi\dot{p}_T(\vec{x}, t) = \int \left[ \frac{\rho_0(\dot{U}_n + U_n)}{r(1 - M_r)^2} \right] dS + \int \left[ \frac{\rho_0 U_n \{r\dot{M}_r + C_0(M_r - M^2)\}}{r^2(1 - M_r)^3} \right] dS \tag{22}$$

$$4\pi\dot{p}_L = \int \frac{1}{C_0} \left[ \frac{L_r}{r(1 - M_r)^2} \right] dS + \int \left[ \frac{L_r - L_M}{r^2(1 - M_r)^2} \right] dS + \frac{1}{C_0} \int \left[ \frac{L^2 \{r\dot{M} + C_0(M_r - M^2)\}}{r^2(1 - M_r)^3} \right] dS \tag{23}$$

where,

$$U_r = v_i + \frac{\rho}{\rho_0}(u_i - v_i) \tag{24}$$

$$L_r = P_{ij}\hat{n}_j + \rho u_i(u_n - v_n) \tag{25}$$

The details procedure of the solution is described in [60]. The governing equations are solved using the pressure-velocity coupling and transient Semi-Implicit Method for Pressure-linked Equations-Consistent (SIMPLEC) algorithm within the scFLOW2Actran software. This algorithm, an extension of the SIMPLE algorithm, is employed to enhance the accuracy of pressure correction in pressure-velocity coupling calculation [61,62]. It is specifically designed to be robust and efficient, particularly for incompressible flow and flows with recirculation [63]. This chosen algorithm is well-suited for both aerodynamic and aeroacoustic applications [62]. The sound pressure level (SPL) in decibels is determined using the reference acoustic pressure  $p_{ref} = 2 \times 10^{-5}$  Pa. The equation of this reference is expressed as follows:

$$SPL = 20 \log_{10} \left( \frac{p'}{p_{ref}} \right) \tag{26}$$

### 2.4 Computational Aero-acoustic Setup and Numerical Grid

The schematic diagram of the whole computational domain used for the microphone port in Figure 2 has dimensions of 0.2 m ( $WI$ ) x 0.4 m ( $DI$ ) x 0.8 m ( $LI$ ), which closely resemble the dimensions of the test section in the experimental setup. The microphone port cavity itself is scaled up to dimensions of 0.017 m ( $L$ ) x 0.02 m ( $D$ ) x 0.2 m ( $W$ ). The octree (structured mesh) and polyhedral mesh are depicted in Figure 3. The octree structure, developed by Finkel and Bentley [64] and Yerry and Shephard [65] was utilized for mesh generation purposes. The size of the octree was determined based on the resolution of the results, taking into account the calculation time and memory consumption. This structure allowed full flexibility for the refinement level of the cells [66]. A polyhedral mesh (arbitrary polyhedral) was also employed to enhance stability and computational time accuracy [67]. Two sets of wall prisma layers were defined at the cavity surface with a thickness of 0.2. The time step size for LES simulation is set at 0.001s with the requirement to keep the Courant-Freidrichs-Lewy (CFL) number [68] below 1. The CFL conditions help to ensure numerical stability by relating the time step to the spatial discretization grid size and the speed of the information propagation in the system [69, 70]. The CFL condition is expressed as:

$$CFL = \frac{u \cdot \Delta t}{\Delta x} \leq 1 \tag{27}$$

where  $u$  is the flow velocity,  $\Delta t$  is the time-step,  $\Delta x$  is the spatial grid size, and 1 is the maximum allowable CFL number. The total computational time was approximately 5 hours.

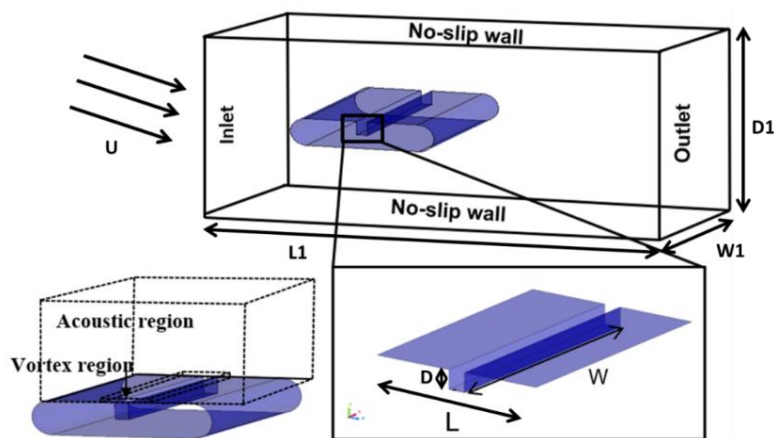


Figure 2. Schematic diagram of the computational domain and boundary conditions

### 2.5 Mesh Independent Study

A mesh-independent test was conducted to ensure simulation accuracy while optimizing computational resources. Figure 4 shows the three different mesh grid sizes for the CAA simulation. Table 1 describes the details of mesh grid resolution schemes. Particular attention was paid to mesh resolution to the mesh refinement at the cavity location. Figure 5 compares the computational results for sound pressure level against the number of cells among three different meshes. It was observed that the computational result of the sound pressure level is approximately 5 dB higher than the coarse mesh. However, the sound pressure level for fine and medium meshes is nearly identical, differing by approximately 1 dB. The results also indicate the sound pressure level for the fine mesh aligns with the actual measurement of 85 dB at a wind speed of 0.8 m/s. However, the computational time required for this mesh scheme was the longest. Therefore, the medium -mesh was selected for the next simulation to ensure computational accuracy and efficiency [71].

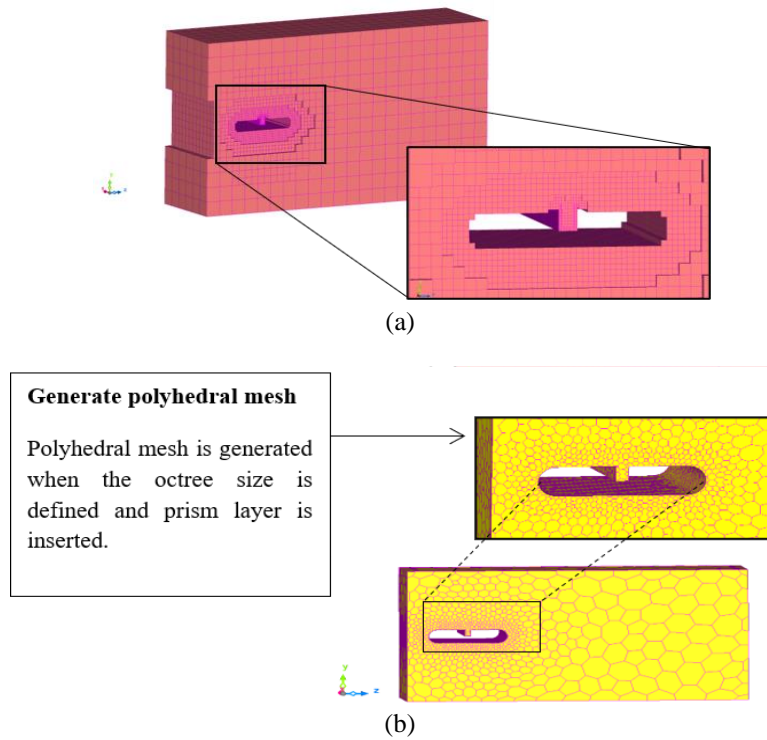


Figure 3. (a) Octree structure mesh and (b) Polyhedral mesh of the microphone port

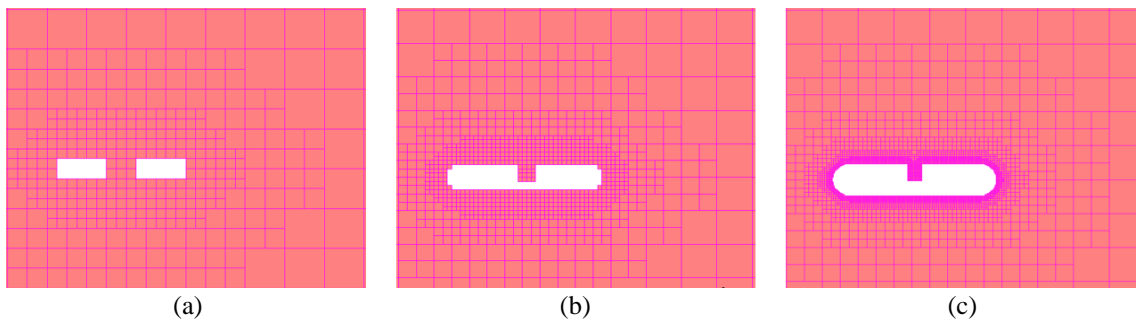


Figure 4. Types of mesh grid of the computational domain: (a) coarse, (b) medium and (c) fine

Table 1. Grid mesh parameters for three mesh grid resolutions

Mesh	Mesh size (mm)	Number of mesh elements	Sound Pressure Level (dB)
Coarse	0.01	41918	89
Medium	0.005	132443	86
Fine	0.001	1477178	85

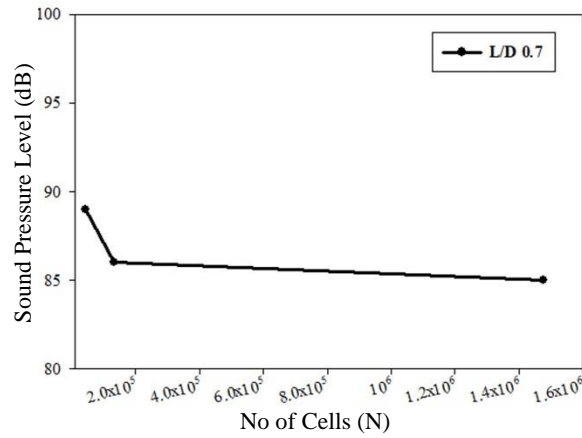


Figure 5. Mesh independence study

### 2.6 Grid Convergence Study

To quantify the efficiency and accuracy of grid convergence study for the CFD simulation, two methods are utilized; generalized Richardson exploration (RE) and grid convergence index (GCI). These approaches lean more towards quantitative judgment for grid independence assessment, providing a more systematic, accurate, and rigorous method for assessing grid independence [72]. The computational grid resolution is divided into three: coarse, medium, and fine, as shown in Figure 4. The criterion commonly used in determining grid independence is monotonic behavior. The key parameters of sound pressure level are monitored as the grid size is successively refined. The parameter should exhibit a monotonic trend, indicating that the iterative process is steadily and reliably approaching a final desired solution [73]. Since this study involved three-dimensional (3D), the refinement ratio for the grid size can be defined by the average cell size,  $h$ . The calculation of average cell size,  $h$  is as follows:

$$h = \left[ \frac{1}{N_{cell}} \sum_{i=1}^{N_{cell}} (\Delta V_i) \right]^{1/3} \tag{28}$$

where  $N_{cell}$  is the total number of cells,  $\nabla V_i$  is the volume of the  $i^{th}$  cell. Based on Table 2, the refinement ratio between two grid mesh size resolutions of  $r_{n+1,n}$  is calculated using the following equation [74].

$$r_{n+1,n} = \frac{NC_{n+1}}{NC_n} \tag{29}$$

The grid refinement ratio of two grid mesh resolution  $r_{21}$  and  $r_{32}$  are 2.2 and 1.46. The RE [75] method is a method to estimate the continuum value from a series of lower-order values such as the grid mesh size approaching zero ( $h \rightarrow 0$ ). It is generalized into  $p^{th}$  method [76]. The calculation is expressed as:

$$f_{RE} \approx f_1 + \left[ \frac{f_1 + f_2}{r^p - 1} \right] \tag{30}$$

According to [77], the order of accuracy,  $p$  can be estimated by the following equation:

$$p = \frac{\ln \left( \frac{\epsilon_{32}}{\epsilon_{21}} \right)}{\ln(r)} \tag{31}$$

$$\epsilon_{32} = f_3 - f_2 \tag{32}$$

$$\epsilon_{21} = f_2 - f_1 \tag{33}$$

The extrapolated values are determined based on their convergence ratio,  $R$ . The convergence ratio can be described as:

$$R = \frac{\epsilon_{21}}{\epsilon_{32}} \tag{34}$$

Three conditions are commonly used for this solution [78]:

- i)  $R < 0$  for oscillatory convergence
- ii)  $0 < R < 1$  for monotonic convergence
- iii)  $R > 1$  for monotonic divergence

The GCI method evaluates the estimation error and convergence solution obtained from the generalized Richardson extrapolation theory. The GCI calculated as

$$GCI_{i+1,i} = F_s \left| \frac{\varepsilon_{i+1,i}}{r^p - 1} \right| \times 100 \% \tag{35}$$

where  $F_s = 1.25$  is a safety factor for three mesh grid sizes proposed by [79]. The discrepancy between the simulation value and the extrapolation value is used to define the estimation errors given as follows:

$$E_i = \frac{f_1 - f_{RE}}{f_{RE}} \times 100 \% \tag{36}$$

The GCI is a widely used technique in CFD and numerical analysis to evaluate the convergence of numerical solutions obtained through grid refinement studies. It is applied to each grid resolution to access the discretization error achieved by reducing the grid size, as predicted by the Richardson extrapolation theory [79,80]. Table 2 presents the results of order accuracy and the GCI value of three different mesh resolutions. According to the table, it can be observed that the GCI value decreases as the grid is refined ( $GCI^{21} < GCI^{32}$ ). The grid convergence analysis demonstrates a convergence rate of approximately 0.298 % with three different refined grid meshes, indicating a monotonic reduction in uncertainties ( $0 < R < 1$ ). This finding aligns with the expectation of Ali et al. [81]. However, considering the higher computational load associated with the fine mesh [71], a medium-mesh with a size of 0.005 mm was chosen for the subsequent CAA analysis. The GCI value for the medium mesh remains within an acceptable range, below 2 %. The comparison of GCI and percentage error for the noise level among the three mesh resolutions is presented in Figures 6(a) and (b). The results indicate that the fine grid resolution closely approximates the extrapolated value, resulting in a smaller error percentage compared to the other grid resolutions.

Table 2. Grid convergence uncertainty estimation in CFD simulation

	$f_1$	$f_2$	$f_3$	$f_{RE}$	$ \varepsilon_{21} $	$ \varepsilon_{32} $	$R$	$GCI^{21}(\%)$	$GCI^{32}(\%)$
Value	84	85	89	83.7	1	4	0.25	0.49	1.98

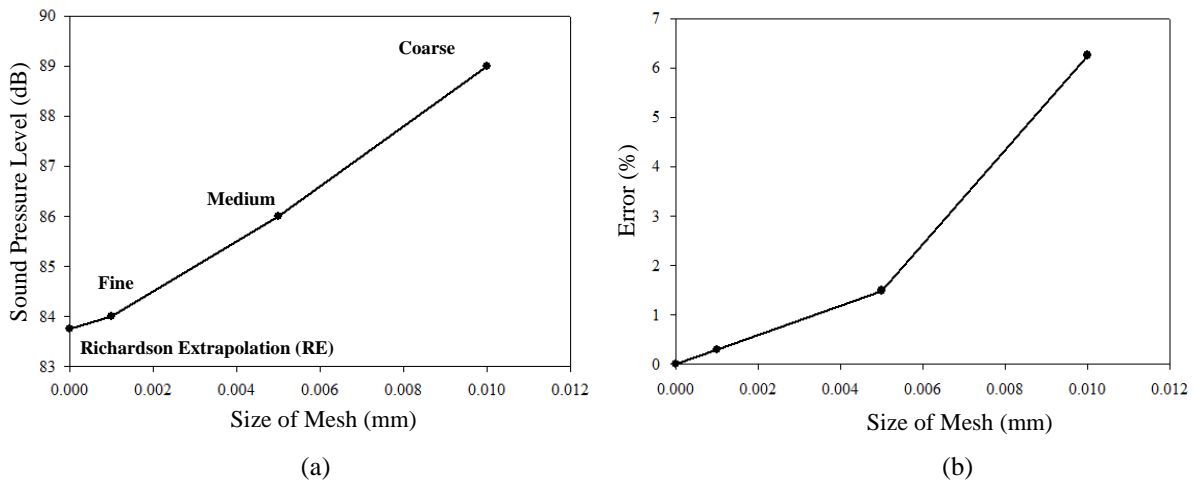


Figure 6. Grid convergence uncertainty estimation for microphone port: (a) the sound pressure level and (b) discrepancy errors of GCI

### 2.7 Boundary Conditions

The wind speeds of 0.8 m/s, 2.2 m/s, and 4.4 m/s corresponding to Reynolds numbers 7831, 25453, and 43083, respectively, are set at the inlet of the computational domain. The outlet is set as a pressure outlet. The model microphone port is set under no-slip conditions. To prevent any contamination of sound waves and reflection at the inlet and outlet, an infinite acoustic region (non-reflection) is introduced at both ends of the fluid domain. The outlet boundary is positioned well downstream of the cavity edge to eliminate the influence of pressure reflections from the outflow boundary [82]. The material model employed for the fluid and acoustic domain analysis assumes air to be incompressible, suitable for conditions involving low wind speeds and small pressure variations, at a temperature of 20°C. The sound speed in the domain is 343.7 m/s, with a density of 1.206 kg/m<sup>3</sup>. The study excludes consideration of diaphragm system vibrations. To enhance a better understanding of the sound generation and propagation of the microphone port, a set of monitoring points are strategically placed within the port and the wall at different distance radii of 0.2 m and 0.4 m. The far-field monitoring points at these different distance radii of 0.2 m and 0.4 m are depicted in Figure 7. Each monitoring point is set at an angular interval of 10°. Four observation angles ( $\theta$ ) are considered: 0°, 45°, 90°, and 135°, each with a 45° angular interval. A receiver point, denoted as P0 and representing the noise source is positioned to align with the experimental test setup.

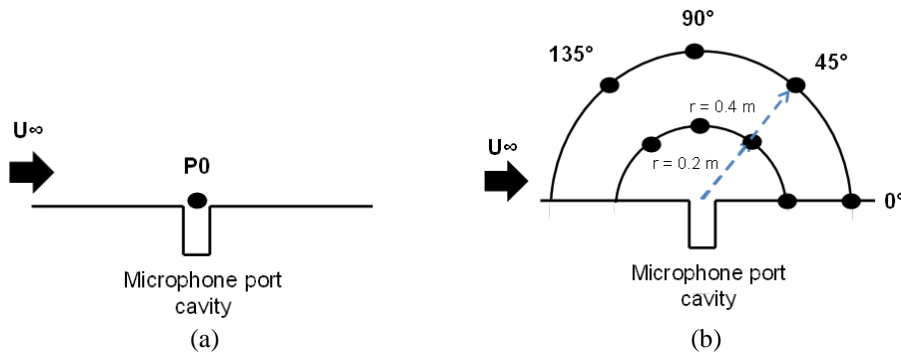


Figure 7. The monitoring point of (a) near field and (b) far-field at different orientation angle microphone location

### 2.8 Solution conditions

The hybrid co-simulation of aeroacoustic analysis in scFLOW2Actran is conducted in three steps. Firstly, a steady-state calculation of the flow field using the RANs ( $k - \omega SST$ ) turbulence model. This model is widely used and demonstrates good prediction capabilities for adverse pressure gradients and flow separation [45]. However, it only resolves the time-averaged flow and does not account for the frequency term, making it unsuitable for capturing the flow-induced noise. The steady-state simulation is run for 400 cycles until the residuals are converged. In the second step, the LES-WALE is utilized for transient calculation. The time step for this transient calculation is set to 2000 cycles with a time step of 0.001 s. The LES-WALE is chosen for the SGS model due to its good performance in simulating the swirling and separating-reattaching flows in the pre-transition regime from laminar to turbulent flow [83]. Additionally, this model is used to correct any wall turbulence model errors [84]. The fluid session is activated once the LES-WALE analysis is converged and concludes with the last cycle at 3000, using a time step of 0.0001s. A CMB file is generated as the output of the fluid session, and this file is later used to interpolate with the acoustic file configuration. The third step involves establishing a new project for the acoustic session. In this session, acoustic boundary conditions and properties such as monitoring points (receiver), infinite element (IE), and filter distance are set in the Actran module. The IEs are placed at the inlet and outlet boundaries to represent the acoustic non-reflection boundary condition, and the filter distance for the acoustic sound source is set to 0.05 m. The acoustic analysis starts at 2.0001s and ends at 2.1s with an interval time of 0.0001s. An iCFD file is generated as the output of the acoustic session, and the Actran software utilizes this file to extract the acoustic source through a fast Fourier transform algorithm. A Fast Fourier transform is performed using the Hanning window to convert the time domain into the frequency domain. Finally, the MUMPs solver in scFLOW2Actran simultaneously computes the solutions for the output CMB file and iCFD file. This MUMPs solver is known for its minimal memory requirement and fast computation [71]. These step modules are illustrated in Figure 8.

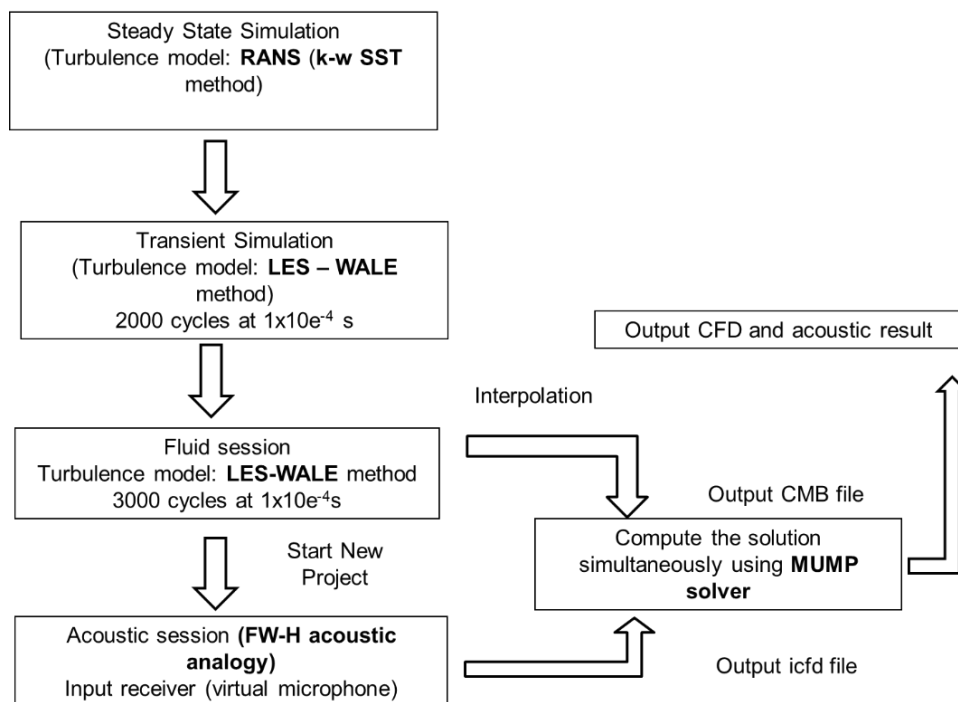


Figure 8. The flowchart of the direct-hybrid co-simulation computational aeroacoustic analysis in scFLOW2Actran

## 2.9 Experimental Validation

The validation test for the microphone port was conducted within a small wind tunnel at the Aerodynamics Laboratory of Universiti Sains Malaysia (USM). The experimental setup in the small wind tunnel is illustrated in Figure 9. An open cavity length-to-depth ( $L/D$ ) of 0.7 was employed for the model cavity. It is important to note that the wind tunnel test section is not anechoic. To mitigate this, foam wedges were installed inside the test section to absorb the background noise. However, as the test was not conducted in a real anechoic room, the measured results were about 7-9 dB higher than the background noise level [85]. Sound pressure measurements were carried out using a microphone in conjunction with an IMC data analyzer. The monitoring point, P0, corresponding to  $0^\circ$  degrees, was selected to validate the accuracy of the simulation method.

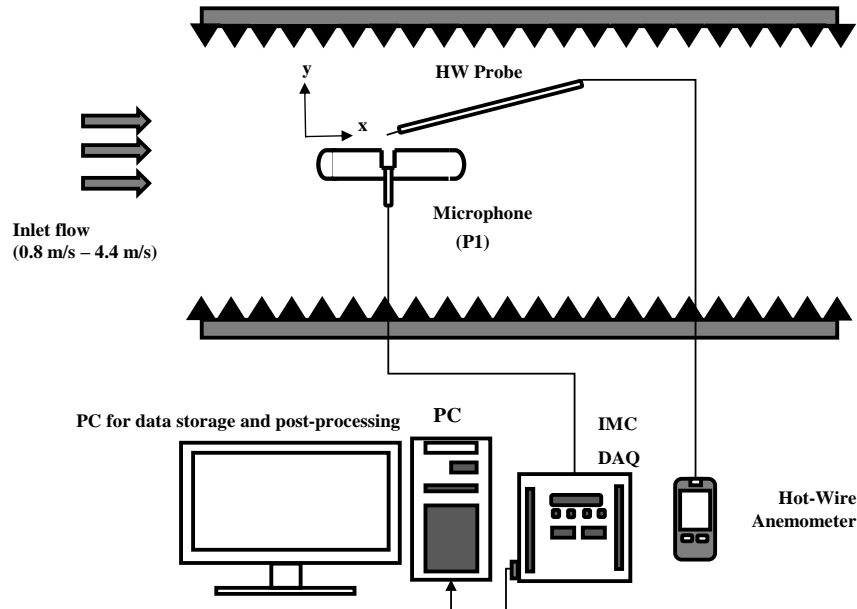


Figure 9. Schematic diagram of the experimental setup for sound measurement

## 3. RESULTS AND DISCUSSION

### 3.1 Validation Test Case

Figure 10 compares the experimental test, and simulated sound pressure levels at monitoring points (P0) for a wind direction  $0^\circ$ . The wind noise spectrum exhibits a peak between 20 Hz and 500 Hz, with an amplitude of approximately 120 and 117 dB for both experimental test and simulation, respectively. The wind noise spectrum of the cavity in the experimental test is approximately 3 dB, corresponding to 2.5 % higher than the simulated noise level. The results indicate a similar trend pattern between the predicted simulation and experimental data. The measurements were conducted according to ISO 3744 standards [86], providing valuable wind noise data for the test model. The frequency response of the measured data is consistent with the low-frequency characteristics reported by [87]. The small discrepancies between the experiment test and simulated values can be attributed to factors such as wind instability, backflow noise, and the positioning of the microphone at a distance [88]. Thus, the reliability of the current CAA simulation results can be affirmed. Table 3 provides the comparison noise level between simulated and measured at a frequency of 24 Hz.

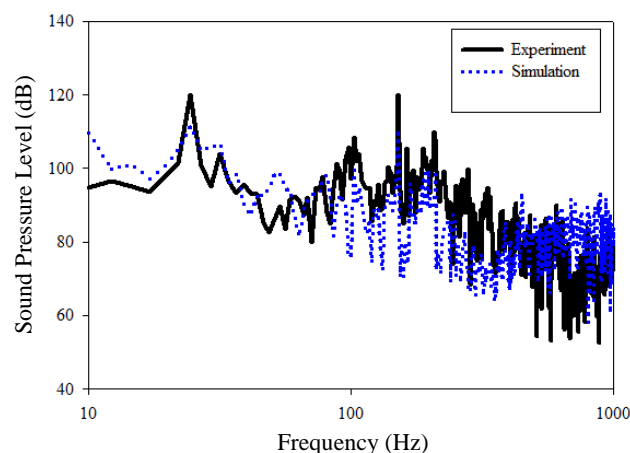


Figure 10. Comparison of SPL between simulation and experiment test at P0 under wind speed of 4.4 m/s for cavity ratio of 0.7

Table 3. Comparison of the SPL between simulation and experimental at P0

Sound Pressure Level (dB) at a frequency of 24 Hz	
Simulation results	120
Experimental results	117
Differences	3

### 3.2 Noise Characteristics

The near-field noise generated by the cavity length-to-depth (L/D) ratio of 0.7 was first measured. Figure 11 shows the noise spectrum at the P0 in the base of the cavity at wind speed  $U = 4.4$  m/s. The noise spectra exhibit three frequency modes; the first dominant frequency peak mode (mode-1) at  $f_1 = 24$  Hz, second mode (mode-2) at  $f_2 = 102$  Hz, and the third mode (mode-3) at  $f_3 = 151$  Hz. The dominant frequency  $f_1$  has an amplitude of 12 dB and 1.1 dB higher than the frequency  $f_2$  and  $f_3$ , indicating that the dominant sound source of wind-induced noise is mainly under low frequencies below the range of 250 Hz. These typical cavity oscillation incompressible flows are described in early studies [89-93]. This is also agreed by [87] who described the range of wind-induced noise as particularly under the low-frequency range of 20 Hz to 250 Hz. Table 4 provides the quantitative comparison of the simulated and measured shedding frequencies and their 2<sup>nd</sup> and 3<sup>rd</sup> harmonics modes.

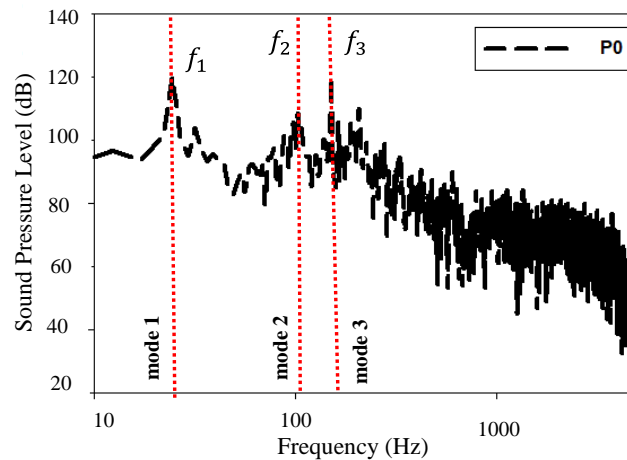


Figure 11. Noise spectrum of the cavity length to depth ratio of 0.7 at wind speed,  $U = 4.4$  m/s under P0

Table 4. Comparison of the simulated and experimental frequencies for the microphone port at P0

	Shedding frequency (Hz)	Second harmonic	Third harmonic
Simulation	24	102	151
Experiment	24	101	146
Differences	0%	-0.9%	-3.4%

### 3.3 Noise Map Identification

The noise map identification using direct-hybrid CAA co-simulation in scFLOW2Actran is shown in Figure 12 at varied frequencies for the near-field distances radii,  $r$  of 0.2 m and 0.4. The sound pressure level was observed to be the lowest at  $r = 0.4$  m for all frequencies, indicating that it corresponds to the farthest distance from the wind source and experiences less flow separation over the microphone port region. The primary noise source was identified at the opening microphone port, specifically at the leading edge, inner region, and trailing edge of the cavity port where the flow interacts with the wall. The noise exhibited a low frequency of around 20 to 1000 Hz. It can be observed that the highest noise levels were recorded at frequencies of 22 Hz, 44 Hz, 55 Hz, 144 Hz, 255 Hz, 366 Hz, and 1132 Hz, corresponding to sound pressure levels of 136dB, 126 dB, 116 dB, 106 dB, 97.5 dB, 98.6 dB, and 86.4 dB, respectively, at distance  $r = 0.2$  m. Meanwhile, a distance  $r = 0.4$  m provides a noise level lower than a distance  $r = 0.2$  m. The noise gradually decreased with increasing frequencies; particularly beyond 1132 Hz. Table 5 provides a summary of the differences between the two distances.

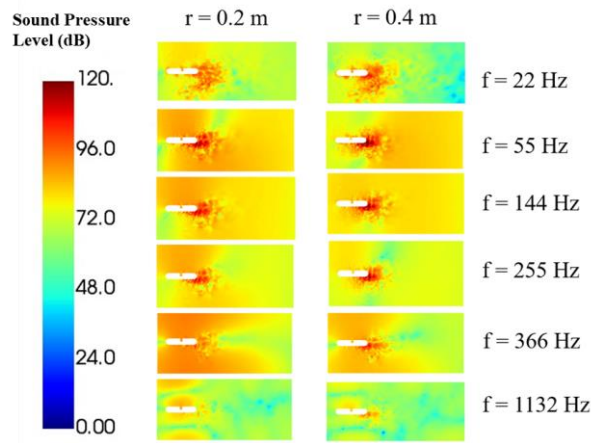


Figure 12. Noise source map identification at wind speed 4.4 m/s for different distances radii,  $r = 0.2$  m and 0.4 m at P0

Table 5. Sound pressure level at different frequencies with two varied distance radii

Frequency (Hz)	Sound Pressure Level (dB)		Error (%)
	Distance radii, $r$ (m)		
	0.2	0.4	
22 Hz	136	133	2
44 Hz	126	119	5
55 Hz	116	114	1.7
144 Hz	106	101	4.7
255 Hz	97.5	92	5.6
366 Hz	98.6	90.2	8.5
1132 Hz	86.4	81	6.2

### 3.4 Influence of Distance Radii

The noise spectra at varied wind speeds,  $V = 0.8$  m/s, 2.2 m/s, and 4.4 m/s with different distance radii are shown in Figure 13(a) and (b). The graphs illustrate that the broadband noise level increases with higher wind speed. Notably, a peak frequency response is marked by the presence of wind-induced noise in all cases. The peak sound pressure levels at a distance,  $r$  of 0.2 m range from about 51 dB to 98 dB at a frequency of 366 Hz. Similarly, the peak sound pressure levels at  $r$  of 0.4 m range from around 51.1 dB to 90.2 dB. It is noteworthy that the sound pressure level at a distance of 0.4 m decreases is approximately 0.1 dB to 8 dB lower than at a distance radii,  $r$  of 0.2 m. This decrease in sound pressure level at a distance radii of 0.4 may be attributed to the receiver being farther away from the noise source. The distance radius of 0.4 m exhibits the minimum sound pressure level compared to the distance radius of 0.2 m at a wind speed of 4.4 m/s, highlighting the impact of the receiver’s proximity to the noise source, as depicted in Figure 14.

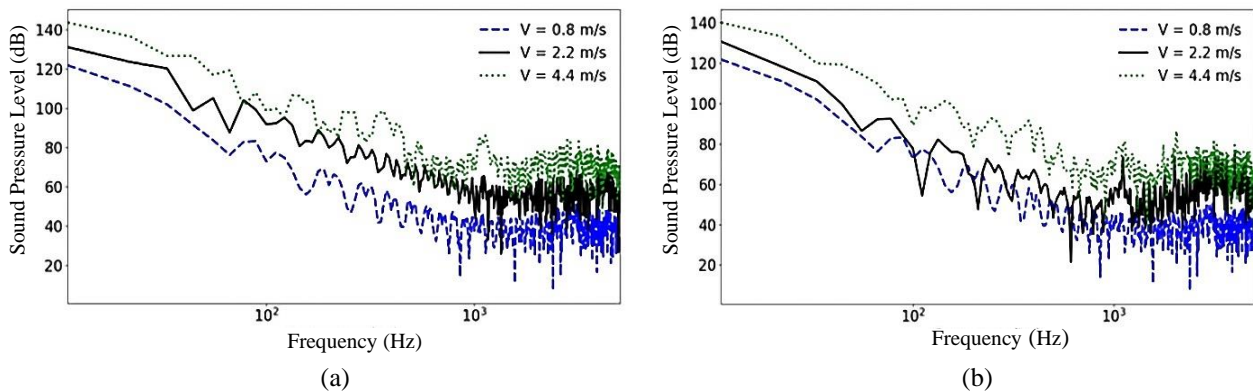


Figure 13. Comparison of sound pressure levels (dB) at various wind speeds 0.8 m/s, 2.2 m/s, and 4.4 m/s of different distance radii: (a)  $r = 0.2$  m and (b)  $r = 0.4$  m

Table 6. Overall sound pressure level of different two distances radi under varied wind speed

Wind speed (m/s)	Overall Sound Pressure Level (dB)		Error (%)
	Distance radii, $r$ (m)		
	0.2	0.4	
0.8	130	129.9	0.7
2.2	140	138	1.4
4.4	152	149.1	1.9

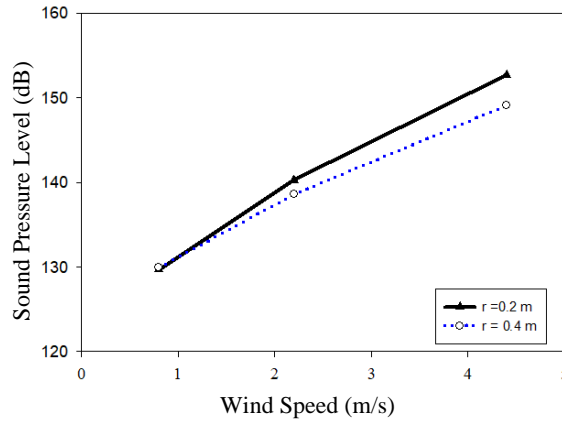


Figure 14. Comparison of sound pressure level versus wind speed under different distance radii

Figures 15(a) and (b) show the far-field noise directivity of the microphone port cavity at peak frequencies of 24 Hz, and 399 Hz. It can be seen that a monopole pattern is observed at wind speed of 0.8 m/s for both frequencies. However, when both frequencies are at higher wind speeds, the dipole patterns are shown. It shows that the microphone port cavity is a dipole sound source it is the main contributor to the wind-induced noise. This is due to the interaction between wind and structural microphone port. The directivity pattern is associated with a dipole, dominating the result for both distance radii. These findings align with previous studies [94], which state that the noise source is the dipole source generated by the vortex shedding and pressure fluctuation. The SPL values of receiving points at a frequency of 24 Hz are larger than that of receiving points at a frequency of 366 Hz. The sound pressure level value of receiving points from 0° to 10° are larger than other receiver points. It indicates that far-field noise directivity has a stronger directivity in that flow direction. Table 6 provide the overall sound pressure level of two different distance radii,  $r$  at varied wind speed.

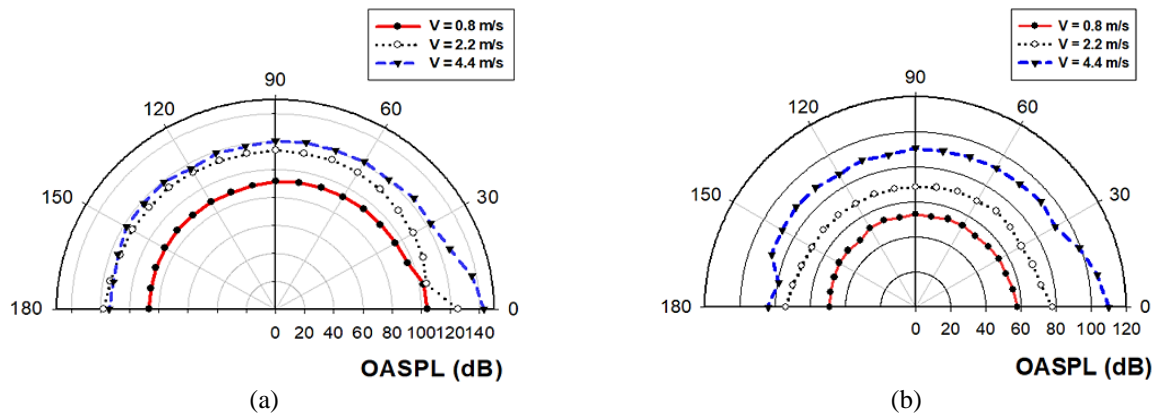


Figure 15. Far-field noise directivity for different wind speeds of 0.8 m/s, 2.2 m/s 4.4 m/s under frequencies of: (a) 24 Hz and (b) 399 Hz

### 3.5 Influence of Wind Orientation Angle

Figure 16 shows the noise spectra at airflow orientation angles at (0°, 45°, 90°, and 135°) with different distance radii ( $r = 0.2$  and  $0.4$  m) at a wind speed of 4.4 m/s. This comparison was to investigate the influence of distance when compared to a different orientation angle. The spectrum reveals several multiple peak frequencies within the range between 20 Hz to 4000 Hz. Broadband results exhibit a consistent pattern for both distances with the distance radii of 0.2 m showing a slightly higher noise level compared to the distance radii of 0.4 m. Notably, at an angle of 0°, the noise level is higher for both distances radii, as depicted in Figure 17. At a distance of 0.2 m, the noise level at approximately 2.8 dB higher than at a distance radii ( $r$ ) of 0.4 m at a 0° angle. The broadband noise is higher at  $\theta = 0^\circ$  and lowest at  $\theta = 135^\circ$ , indicating a significant influence of the observation angle on the wind-induced noise level at the microphone port.

Figure 18 shows the far-field noise directivity for the observer angle at a two-distance radius i.e.;  $r = 0.2$  m and  $0.4$  m from the center of the cavity under a wind speed of  $4.4$  m/s. It is observed that the sound pressure level at a distance radius ( $r$ ) of  $0.2$  m is higher than at a distance radius ( $r$ ) of  $0.4$  m. This suggests that the acoustic wave gradually increased with a near distance of the source of noise [95]. This figure also reveals that the obvious directivity location can be observed for both distances at  $0^\circ$  and  $45^\circ$  intervals, with  $2.9$  dB and  $4.9$  dB differences, respectively. Table 7 provides the comparison of overall sound pressure levels at different orientation angles at two distance radii.

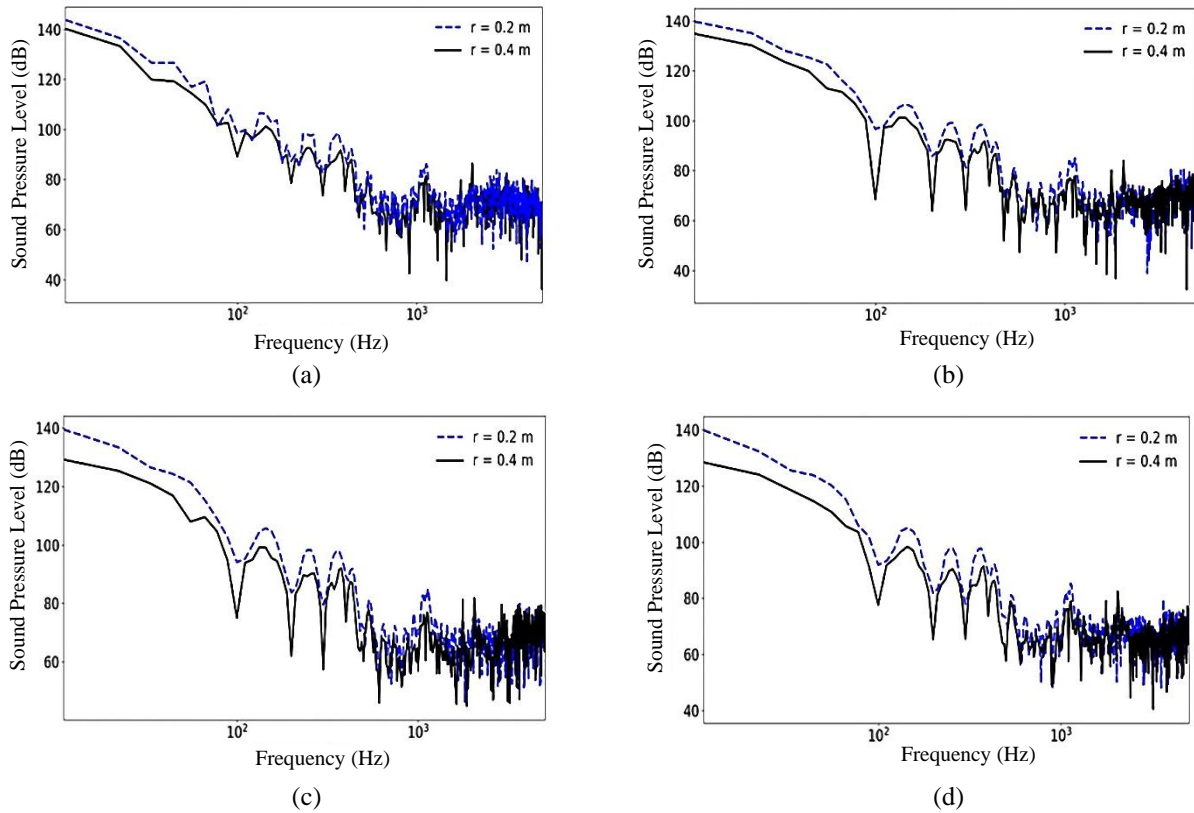


Figure 16. Comparison of noise spectra with different distance radii ( $r = 0.2$  m and  $0.4$  m) for different orientation angles (a)  $0^\circ$ , (b)  $45^\circ$ , (c)  $90^\circ$  and (d)  $135^\circ$  at a wind speed of  $4.4$  m/s

Table 7. Sound pressure level at different orientation angles

Orientation angles, $\Theta$ ( $^\circ$ )	Overall Sound Pressure Level (dB)		Error (%)
	Distance radii (m)		
	0.2	0.4	
0	152	149.1	1.9
45	150	145.1	3.2
90	149.2	140.2	6
135	148.9	138.9	6.7

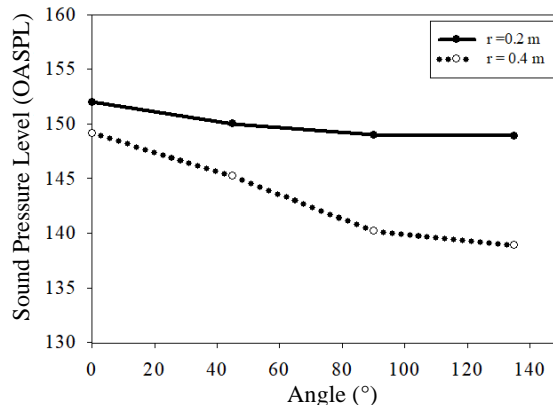


Figure 17. Comparison sound pressure angle at different angles ( $0^\circ$ ,  $45^\circ$ ,  $90^\circ$  and  $135^\circ$ ) of two varied distance radii,  $r$

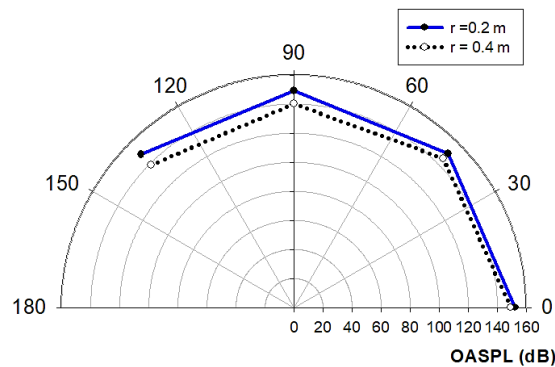


Figure 18. Far-field noise directivity under different distance radii ( $r = 0.2$  m and  $0.4$  m) at wind speed of  $4.4$  m/s

#### 4. CONCLUSIONS

Computational aeroacoustics modeling of the microphone port of two-way radio was successfully conducted and validated with experimental tests. The results are summarized below:

- i) The direct-hybrid co-simulation CAA approach for analyzing the wind-induced noise of the microphone port was implemented in this study. A comparison was made between the results and the sound measurement test. The deviation between the simulated results and experimental data was approximately 2.5 %, indicating the feasibility of the proposed co-simulation CAA method.
- ii) The reliability of the numerical simulation was verified and an error reduction of 2 % was achieved by implementing the RE and GCI techniques.
- iii) The noise source map identification was performed by observing the shedding vortices at the opening, including the leading-edge, inside, and trailing edge of the cavity, using CAA simulation.
- iv) The parametric analysis revealed that wind-induced noise of the microphone port cavity depends on the orientation angle (wind direction) and wind speed. The highest noise was observed when the wind came from the front and at high speeds. Increasing the wind speed from  $0.8$  m/s to  $4.4$  m/s resulted in a 1-3 dB increase in wind noise.
- v) The comparison of far-field noise directivity between distance radii of  $0.2$  m and  $0.4$  m shows a completely different behavior observed at different wind speeds and frequencies. As the distance radii increases with increasing speed, the noise radiated decreases. The observed noise directivity pattern corresponds to a dipole pattern, in a direction angle of  $0$  to  $45^\circ$ , which is expected the source of wind-induced noise.

The proposed direct-hybrid co-simulation CAA approach provided valuable insights into the spatial distribution of noise sources, aiding in the understanding of the acoustic characteristics associated with microphone port cavity flow. These results serve as a crucial tool for researchers and engineers to predict and mitigate unwanted noise effects in cavity flow scenarios. Additionally, it can be applied in any flow acoustic coupling application.

#### 5. ACKNOWLEDGMENTS

The author would like to express her gratitude to Universiti Teknologi Malaysia (UTM) for allowing the use of their student edition co-simulation ScFLOW2Actran to perform the aeroacoustics analysis. This study was supported by the Research University Individual Grant (RUI) via Grant No: 001/PAERO/8014005.

#### 6. REFERENCES

- [1] E. Nemer, W. Leblanc, "Single-microphone wind noise reduction by adaptive postfiltering," in *IEEE Workshop on Applications of Signal Processing to Audio Acoustic*, pp. 177–180, 2009.
- [2] L. Håkansson, S. Johansson, M. Dahl, P. Sjösten. *Noise Canceling Headsets for Speech Communication: Noise Reduction in Speech Applications*, 1st ed. United States: CRC Press, 2002.
- [3] P. Yamkovoy, "Wind noise mitigation in active noise cancelling headphone system and method," US Patent 10582293B2, 2020.
- [4] G. W. Lyons, "As the wind blows: Turbulent noise on outdoor microphones," *Acoustic Today*, vol. 17, no. 4, pp. 20-28, 2021.
- [5] M. Wang, D. Angland, X. Zhang, "The noise generated by a landing gear wheel with hub and rim cavities," *Journal of Sound and Vibrations*, vol. 392, pp. 127–141, 2017.
- [6] E. Neri, J. Kennedy, G. J. Bennett, "Bay cavity noise for full-scale nose landing gear: A comparison between experimental and numerical results," *Aerospace Science Technology*, vol. 72, no.11, pp. 278–291, 2018.

- [7] Y. Zhang, H. Chen, K. Wang, M. Wang, "Aeroacoustic prediction of a multi-element airfoil using wall-modeled large-eddy simulation," *AIAA Journal*, vol. 55, no. 12, pp. 4219–4233, 2017.
- [8] A. E. Şeker, B. Zafer, I. Gonzalez-Martino, M. Yüçetepe, "Aeroacoustic investigation of transonic flow behavior in M219 deep cavity with passive flow control configurations," *Physics of Fluids*, vol. 35, no. 10, p. 105117, 2023.
- [9] Y. Wang, Y. Deng, Z. Yang, T. Jiang, C. Su, X. Yang, "Numerical study of the flow-induced sunroof buffeting noise of a simplified cavity model based on the slightly compressible model," *Proceedings of the Institution Mechanical Engineering. Part D: Journal of Automobile Engineering*, vol. 227, no. 8, pp. 1187–1199, 2013.
- [10] Q. Zhang, Y. He, Y. Wang, Z. Xu, Z. Zhang, "Computational study on the passive control of sunroof buffeting using a sub-cavity," *Applied Acoustic*, vol. 159, p. 107097, 2020.
- [11] H. Kim, Z. Hu, D. Thompson, "Unsteady aerodynamics of high speed train pantograph cavity flow control for noise reduction," in *22nd AIAA/CEAS Aeroacoustics Conference*, Lyon, France, 2016, pp. 1-10.
- [12] H. Kim, Z. Hu, D. Thompson, "Effect of cavity flow control on high-speed train pantograph and roof aerodynamic noise," *Railway Engineering Sciences*, vol. 28, no. 1, pp. 54–74, 2020.
- [13] U. Masyitah, M. Fisol, Z. M. Ripin, N. A. Ismail, A. A. Saad, M. Khairul, "Wind noise analysis of a two-way radio," in *IEEE International Conference on Smart Instrumentation, Measurement and Applications (ICSIMA)*, Kuala Lumpur, Malaysia, 2013, pp. 1–5.
- [14] U. M. Fisol, "Experimental and computational fluid dynamics (CFD) analysis of wind-induced noise in two-way radio," *Master Thesis*, Universiti Sains Malaysia (USM), 2016.
- [15] W. M. Hairudin, U. M. Mohd Fisol, N.A. Ismail, "Experimental and numerical analyses of wind-induced noise in two-way radios," *Jurnal Kejuruteraan*, vol. 33, no. 2, pp. 257–264, 2021.
- [16] W. M. Hairudin, "Wind-induced noise inside a microphone's port of a two-way radio", in *INTERNOISE and NOISE CON Congress and Conference Proceedings*, Seoul, Korea, 2020, pp. 2185-2195.
- [17] T. S. Shaw, C. H. Tan, H. T. Yow, "Slim-tunnel wind port for a communication device," US Patent 9877097, 2018.
- [18] W. M. Hairudin, N. M. Kamarudin, O. L. Ean, N. A. Ismail, "An experimental investigation of wind induced noise inside the small cavity in low wind speed," in *IOP Conference Series:Materials Science and Engineering*, vol. 670, p. 012062, 2019.
- [19] W. M. Hairudin, N. M. Kamarudin, L. E. Ooi, N. A. Ismail, "A Qualitative study of the wind noise cavity inside of a two-way radio," in *IOP Conference Series:Material Science and Engineering*, vol. 815, p. 012012, 2020.
- [20] A. Holmberg, "Experimental determination of aeroacoustic sources in low mach number internal flows," *Ph.D Dissertation*, Royal Institute of Technology, Stockholm, 2010.
- [21] X. Gloerfelt, C. Baillywd, D. Juve, "Computation of the noise radiated by a subsonic cavity using direct simulation and acoustic analogy," in *7th AIAA/CEAS Aeroacoustics Conference and Exhibit*, Maastricht, Netherlands, 2001, p. 1-12.
- [22] O. Baysal, G. Yen, K. Fouladi, "Navier-stokes computations of cavity aeroacoustics with suppression devices," *Journal of Vibration and Acoustics*, vol. 116, no. 1, pp. 105-112, 1994.
- [23] S. Arunajatesan, N. Sinha, "Hybrid RANS-LES modeling for cavity aeroacoutics predictions," *International Journal of Aeroacoustics*, vol. 2, no. 1, pp. 65–93, 2003.
- [24] W. De Roeck, G. Rubio, Y. Reymen, J. Meyers, M. Baelmans, W. Desmet, "Towards accurate flow and acoustic prediction techniques for cavity flow noise applications," in *11th AIAA/CEAS Aeroacoustics Conference*, vol. 3, pp. 2241–2252, 2005.
- [25] B. Khanal, K. Knowles, A. J. Saddington, "Computational study of flowfield characteristics in cavities with stores," *Aeronautical Journal*, vol. 115, no. 1173, pp. 669–681, 2011.
- [26] K. Liu, S. Zhou, X. Li, X. Shu, L. Guo, J. Li, et al., "Flow-induced noise simulation using detached eddy simulation and the finite element acoustic analogy method," *Advances in Mechanical Engineering*, vol. 8, no. 7, pp. 1–8, 2016.
- [27] H. Y. Bie, Z. R. Hao, W. Z. An, J. Xu, "Simulations of cavity flow noise and turbulent jet noise using a hybrid method," *Advanceds in Mechanical Engineering*, vol. 8, no. 2, pp. 1–10, 2016.
- [28] Z. Ren, B. Wang, B. Hu, L. Zheng, "Numerical analysis of supersonic flows over an aft-ramped open-mode cavity," *Aerospace Science and Technology*, vol. 78, pp. 427–437, 2018.
- [29] M. Wang, J. B. Freund, S. K. Lele, "Computational prediction of flow-generated sound," *Annual Review of Fluid Mechanics*, vol. 38, pp. 483-512, 2006.
- [30] M. Schlottke-Lakemper, H. Yu, S. Berger, M. Meinke, W. Schröder, "A fully coupled hybrid computational aeroacoustics method on hierarchical Cartesian meshes," *Computer & Fluids*, vol. 144, pp. 137–153, 2017.

- [31] S. Schoder, M. Weitz, P. Maurerlehner, A. Hauser, S. Falk, S. Kniesburgers, et al., “Hybrid aeroacoustic approach for the efficient numerical simulation of human phonation,” *The Journal of Acoustical Society America.*, vol. 147, no. 2, pp. 1179–1194, 2020.
- [32] J. Tyacke, I. Naqavi, Z. Wang, P. Tucker, P. Boehning, “Predictive LES for jet aeroacoustics: Current approach and industrial application,” in *Turbo Expo: Power for Land, Sea, and Air*, Seoul, South Korea, 2016, pp. 1–16.
- [33] S. P. Murugu, A. R. Srikrishnan, B. K. Krishnaraj, A. Jayaraj, A. Mohammad, R. K. Velamati, “Acoustic modeling of compressible jet from chevron nozzle : A comparison of URANS, LES, and DES models,” *Symmetry*, vol. 14, no. 10, p. 1975, 2022.
- [34] S. H. Wasala, S. E. Norris, J. E. Cater, “Numerical simulation and aeroacoustic noise modelling of a wind turbine using a blade section in an annulus,” in *INTERNOISE and NOISE-CON Congress and Conference Proceeding*, no. 8, pp. 1–9, 2014.
- [35] S. H. Wasala, R. C. Storey, S. E. Norris, J. E. Cater, “Aeroacoustic noise prediction for wind turbines using large eddy simulation,” *Journal of Wind Engineering and Industrial Aerodynamic*, vol. 145, pp. 17–29, 2015.
- [36] T. F. Geyer, S. H. Wasala, J. E. Cater, S. E. Norris, E. Sarradj, “Experimental investigation of leading edge hook structures for wind turbine noise reduction,” in *22nd AIAA/CEAS Aeroacoustics Conference*, Lyon, France, 2016, pp. 1–13.
- [37] S. D. Sovani, K. Chen, “Aeroacoustics of an automotive A-pillar rain gutter: A numerical study with the fflowcs-williams hawkins method,” *Noise and Vibration Conference and Exhibition*, Michigan, United States, 2018, pp. 1–10.
- [38] G. Liu, T. Zhang, Y. Zhang, H. Ouyang, X. Li, “Underwater jet noise simulation based on a large eddy simulation/lighthill hybrid method,” *Journal of Acoustical Society America*, vol. 136, no. 4, pp. 2318–2318, 2014.
- [39] S. Hao, H. Yuanan, Y. Xiaowei, D. Shang, “A numerical simulation of flow-induced noise from cavity based on LES and Lighthill acoustic theory,” in *2016 IEEE/OES China Ocean Acoustics (COA)*, Harbin, China, 2016, pp. 1–8.
- [40] Y. Liu, Y. Li, D. Shang, “The hydrodynamic noise suppression of a scaled submarine model by leading-edge serrations,” *Journal of Marine Science and Engineering*, vol. 7, no. 3, p. 68, 2019.
- [41] V. Viitanen, A. Hynninen, T. Sipilä, “Computational fluid dynamics and hydroacoustics analyses of underwater radiated noise of an ice breaker ship,” *Ocean Engineering.*, vol. 279, p. 114264, 2023.
- [42] F. R. Menter, “Two-equation eddy-viscosity turbulence models for engineering applications,” *AIAA Journal*, vol. 32, no. 8, pp. 1598–1605, 1994.
- [43] M. De Gennaro, “Computational fluid dynamics and computational aeroacoustics for turbomachinery applications with emphasis on high speed propellers and vertical axis wind turbines,” *Doctoral Dissertation*, Università degli Studi di Napoli Federico II, Italy, 2010.
- [44] I. A. Ishak, M. S. M. Ali, S. A. Z. Shaikh Salim, “Mesh size refining for a simulation of flow around a generic train model,” *Wind and Structures*, vol. 24, no. 3, pp. 223–247, 2017.
- [45] M. M. Rahman, V. Vuorinen, J. Taghinia, M. Larimi, “Wall-distance-free formulation for SST k- $\omega$  model,” *European Journal Mechanical B/Fluids*, vol. 75, pp. 71–82, 2019.
- [46] M. Kim, J. Lim, S. Kim, S. Jee, D. Park, “Assessment of the wall-adapting local eddy-viscosity model in transitional boundary layer,” *Computational Methods Applied Mechanics Engineering.*, vol. 371, p. 113287, 2020.
- [47] N. V. Nikitin, F. Nicoud, B. Wasistho, K. D. Squires, P. R. Spalart, “An approach to wall modeling in large-eddy simulations,” *Physic of Fluids*, vol. 12, no. 7, pp. 1629–1632, 2000.
- [48] S. B. Pope, “Turbulence Flow,” *Measurement Science and Technology*, vol. 53, no. 9, pp. 1689–1699, 2019.
- [49] M. Lasota, P. Šidlof, M. Kaltenbacher, S. Schoder, “Impact of the sub-grid scale turbulence model in aeroacoustic simulation of human voice,” *Applied Sciences*, vol. 11, no. 4, pp. 1–19, 2021.
- [50] L. Huang, K. Zhao, J. Liang, V. Kopiev, I. Belyaev, T. Zhang, “A numerical study of the wind speed effect on the flow and acoustic characteristics of the minor cavity structures in a two-wheel landing gear,” *Applied Sciences*, vol. 11, no. 23, 2021.
- [51] J. Smagorinsky, “General circulation experiments with the primitive equations I. The basic experiment,” *Monthly Weather Review*, vol. 12, no. 306, pp. 99–164, 1963.
- [52] P. Šidlof, M. Lasota, “Aeroacoustic simulation of human phonation with the wale sub-grid scale model,” in *Proceeding Topical Problems of Fluid Mechanics*, Prague, Czech Republic, 2020, pp. 206–213.
- [53] F. Nicoud, F. Ducros, “Subgrid-scale stress modelling based on the square of the velocity,” *Flow Measurement and Instrumentation.*, vol. 62, pp. 183–200, 1999.
- [54] D. L. Fflowcs Williams, D. L. Hawking, “Sound generation by turbulence and surfaces in arbitrary motion,” *Philosophical Transaction Royal Society London. Series A*, vol. 264, no. 1151, pp. 321–342, 1969.

- [55] C. L. Morfey, C. J. Powles, M. C. M. Wright, "Green's functions in computational aeroacoustics," *International Journal of Aeroacoustics*, vol. 10, no. 2–3, pp. 117–159, 2011.
- [56] E. Molatudi, T. J. Kunene, L. K. Tartibu, "A ffwocs williams-hawkings numerical aeroacoustic study of varied and fixed-pitch blades of an H-rotor vertical axis wind turbine," in *MATEC Web of Conferences*, vol. 347, p. 00013, 2020.
- [57] D. A. Russell, J. P. Titlow, Y. Bemmen, "Acoustic monopoles, dipoles, and quadrupoles: An experiment revisited," *Americal Journal of Physics*, vol. 67, no. 8, pp. 660–664, 1999.
- [58] Y. D. Zhang, J. Y. Zhang, T. Li, L. Zhang, "Investigation of the aeroacoustic behavior and aerodynamic noise of a high-speed train pantograph," *Scientific China and Technology Sciences.*, vol. 60, no. 4, pp. 561–575, 2017.
- [59] T. Li, D. Qin, W. Zhang, J. Zhang, "Study on the aerodynamic noise characteristics of high-speed pantographs with different strip spacings," *Journal of Wind Engineering and Industrial Aerodynamics*, vol. 202, p. 104191, 2020.
- [60] F. Farassat, "Derivation of formulations 1 and 1A of farassat," *Nasa/TM-2007-214853*, pp. 1–20, 2007.
- [61] T.M. Soe, S.Y Khaing, "Comparison of turbulence models for computational fluid dynamics simulation of wind flow on cluster of buildings in mandalay," *International of Journal of Scientific Research Publications*, vol. 7, no. 8, pp. 337–350, 2017.
- [62] L. Yu, S. Diasinos, B. Thornber, "A fast transient solver for low-mach number aerodynamics and aeroacoustics," *Computer and Fluids*, vol. 214, p. 104748, 2021.
- [63] H. Xiao, J. Wang, Z. Liu, W. Liu, "A consistent SIMPLE algorithm with extra explicit prediction — SIMPLEPC," *International Journal of Heat and Mass Transfer*, vol. 120, pp. 1255–1265, 2018.
- [64] J. L. Bentley, R. A. Finkel, "Quad trees a data structure for retrieval on composite keys," *Acta Informatica*, vol. 4, no. 1, pp. 1–9, 1974.
- [65] M. A. Yerry, M. S. Shephard, "Automatic mesh generation for three-dimensional solids," *Computer and Structures*, vol. 20, no. 1–3, pp. 31–39, 1985.
- [66] S. Péron, C. Benoit, "Automatic off-body overset adaptive cartesian mesh method based on an octree approach," *Journal of Computational Physics*, vol. 232, no. 1, pp. 153–173, 2013.
- [67] M. Nur, H. Mat, F. Basir, E. M. Yusup, "Fans deactivation for minimisation of airborne pathogen transmission : During malaysians congregational prayer gathering in mosque," *International Communications and Heat Mass Transfer*, vol. 129, p. 105694, 2021.
- [68] A. J. Robert, F. G. Shuman, J. P. Gerrity, "On partial difference equations in mathematical physics," *Monthly Weather Review.*, vol. 98, no. 1, pp. 1–6, 1970.
- [69] M. Kornhaas, M. Schäfer, D. C. Sternel, "Efficient numerical simulation of aeroacoustics for low mach number flows interacting with structures," *Computational of Mechanics*, vol. 55, no. 6, pp. 1143–1154, 2015.
- [70] K. Kusano, K. Yamada, M. Furukawa, "Aeroacoustic simulation of broadband sound generated from low-mach-number flows using a lattice Boltzmann method," *Journal of Sound and Vibration*, vol. 467, p. 115044, 2020.
- [71] M. N. H. Mat, N. Asmuin, M. F. Md Basir, M. A. Alazwari, M. R. Safaei, "Aeroacoustic analysis of dry ice blasting on divergent nozzle length using CFD to acoustic couple simulation," *Journal of Thermal Analysis and Calorimetry*, vol. 147, no. 11, pp. 6437–6448, 2022.
- [72] S. R. Lizarose Samion, N. H. Shaharuddin, M. S. Mat Ali, "Grid convergence study for detached-eddy simulation of flow over rod-airfoil configuration using openFOAM," in *IOP Conference Series Material Science Engineering*, vol. 491, p. 012023, 2019.
- [73] N. M. Maruai, M. S. M. Ali, M. H. Ismail, S. A. Zaki, "Flow-induced vibration of a square cylinder and downstream flat plate associated with micro-scale energy harvester," *Journal of Wind Engineering and Industrial Aerodynamic*, vol. 175, pp. 264–282, 2018.
- [74] I. B. Celik, U. Ghia, P. J. Roache, C. J. Freitas, H. Coleman, P. E. Raad, "Procedure for estimation and reporting of uncertainty due to discretization in CFD applications," *Journal of Fluids Engineering*, vol. 130, no. 7, p. 078001 2008.
- [75] L. F. Richardson, J.A. Gaunt, "The deferred approach to the limit," *Philosophical transctions of the Royal Society of London: Series A*, vol. 226, pp. 299–361, 1927.
- [76] P. J. Roache, "Perspective: A method for uniform reporting of grid refinement studies," *Journal of Fluids Engineering*, vol. 116, no. 3, pp. 405–413, 1994.
- [77] F. Stern, R. V. Wilson, H. W. Coleman, E. G. Paterson, "Comprehensive approach to verification and validation of CFD simulations—Part 1: Methodology and procedures," *Journal of Fluids Engineering*, vol. 123, no. 4, pp. 793–802, 2001.

- [78] F. Stern, R. Wilson, J. Shao, "Quantitative V&V of CFD simulations and certification of CFD codes," *International Journal of Numerical Methods in Fluids*, vol. 50, no. 11, pp. 1335–1355, 2006.
- [79] D. C. Wilcox. Turbulence Modelling for CFD, 3rd ed. California:DCW Industries, 2006.
- [80] I. Celik, O. Karatekin, "Numerical experiments on application of richardson extrapolation with nonuniform grids," *Journal of Fluids Engineering*, vol. 119, no. 3, pp. 584–590, 1997.
- [81] M. Sukri Mat Ali, C. J. Doolan, V. Wheatley, "The sound generated by a square cylinder with a splitter plate at low reynolds number," *Journal of Sound and Vibration*, vol. 330, no. 15, pp. 3620–3635, 2011.
- [82] T. Hering, J. Dybenko, E. Savory, "Experimental verification of CFD modeling of turbulent flow over circular cavities using FLUENT," in *CSME Forum*, 2006.
- [83] C. Ye, F. Wang, C. Wang, B. P. M. Van Esch, "Assessment of turbulence models for the boundary layer transition flow simulation around a hydrofoil," *Ocean Engineering*, vol. 217, no. 9, p. 108124, 2020.
- [84] C. A. Wagner, S. A. Slimon, "Numerical simulation of non-resonant cavity flow," in *DoD High Performance Computer Users Group Conferences*, Seattle, USA, 2008, pp. 61–68.
- [85] Y. C. Küçükosman, C. Schram, J. V. Beeck, "A remote microphone technique for aeroacoustic measurements in large wind tunnels," *Applied Acoustics*, vol. 129, pp. 346–353, 2018.
- [86] ISO 3744:2010, Acoustics - Determination of sound power levels and sound energy levels of noise sources using sound pressure - Engineering methods for an essentially free field over a reflecting plane," *International Standards Organization: Geneva, Switzerland*, 2010.
- [87] I. Lin, Y. R. Hsieh, P. F. Shieh, H. C. Chuang, L. C. Chou, "The effect of wind on low frequency noise," in *INTERNOISE and NOISE-CON Congress and Conference Proceedings*, Melbourne, Australia, 2014, pp. 1–12.
- [88] W. Yu-qin, D. Ze-wen, "Influence of blade number on flow-induced noise of centrifugal pump based on CFD/CA," *Vacuum*, vol. 172, p. 109058, 2020.
- [89] D. Rockwell, E. Naudascher, "Review-self-sustaining oscillations of flow past cavities," *Journal of Fluids Engineering*, vol. 100, no. 2, pp. 152–165, 1978.
- [90] C. Knisely, D. Rockwell, "Self-sustained low-frequency components in an impinging shear layer," *Journal of Fluid Mechanics*, vol. 116, pp. 157–186, 1982.
- [91] H. Karadogan, D. Rockwell, "Toward attenuation of self-sustained oscillations of a turbulent jet through a cavity," *Journal of Fluids Engineering*, vol. 105, no. 3, pp. 335–340, 1983.
- [92] Y. Yang, D. Rockwell, K. L. F. Cody, M. Pollack, "Generation of tones due to flow past a deep cavity: Effect of streamwise length," *Journal of Fluids and Structures*, vol. 25, no. 2, pp. 364–388, 2009.
- [93] B. A. Tuna, D. Rockwell, "Self-sustained oscillations of shallow flow past sequential cavities," *Journal of Fluid Mechanics*, vol. 758, pp. 655–685, 2014.
- [94] J. Hong, W. Chen, S. P. Wu, "Influence of cavity shape on aerodynamic noise by a hybrid LES-FWH method," *Applied Mechanics and Materials*, vol. 543–547, pp. 358–361, 2014.
- [95] Y. Kang, N. Li, X. L. Huang, C. S. Weng, "Experimental study of the influence of annular nozzle on acoustic characteristics of detonation sound wave generated by pulse detonation engine," *Chinese Physics B*, vol. 31, no. 10, p. 104701, 2022.